Stacking fault energetics of α- and γ-cerium investigated with *ab initio* calculations

A. Östlin,[1,*] I. Di Marco,[2] I. L. M. Locht,[2,3] J. C. Lashley,[2,4] and L. Vitos[1,2,5]

[1]*Applied Materials Physics, Department of Materials Science and Engineering, KTH Royal Institute of Technology, SE-100 44 Stockholm, Sweden*

[2]*Department of Physics and Astronomy, Uppsala University, P.O. Box 516, SE-75120 Uppsala, Sweden*

[3]*Radboud University, Institute for Molecules and Materials, Heyendaalseweg 135, 6525 AJ Nijmegen, The Netherlands*

[4]*Los Alamos National Laboratory, P.O. Box 1663, Bikini Atoll Road, Los Alamos, New Mexico 87545, USA*

[5]*Research Institute for Solid State Physics and Optics, Wigner Research Center for Physics, P.O. Box 49, H-1525 Budapest, Hungary*

(Received 12 December 2014; revised manuscript received 22 December 2015; published 14 March 2016)

At ambient pressure the element cerium shows a metastable ($t_{1/2} \sim 40$ years) double-hexagonal close-packed β phase that is positioned between two cubic phases, γ and α. With modest pressure the β phase can be suppressed, and a volume contraction (17%) occurs between the γ and the α phases as the temperature is varied. This phenomenon has been linked to subtle alterations in the $4f$ band. In order to rationalize the presence of the metastable β phase, and its position in the phase diagram, we have computed the stacking fault formation energies of the cubic phases of cerium using an axial interaction model. This model links the total energy differences between hexagonal closed-packed stacking sequences and stacking fault energetics. Total energies are calculated by density functional theory and by dynamical mean-field theory merged with density functional theory. It is found that there is a large difference in the stacking fault energies between the α and the γ phase. The β-phase energy is nearly degenerate with the γ phase, consistent with previous third-law calorimetry results, and dislocation dynamics explain the pressure and temperature hysteretic effects.

DOI: 10.1103/PhysRevB.93.094103

I. INTRODUCTION

Cerium shows unconventional phase equilibria that have been linked to subtle alterations in the $4f$ band [1–3]. Since the discovery of the unconventional phases by Bridgman nearly 100 years ago [4], there have been numerous papers written on the subject. Although the majority of these papers have focused on the relationship between the electronic structure and the volume (for a review see Ref. [5]), our focus is on the structural differences and the presence of the β phase. At zero pressure, cerium crystallizes in the high-temperature δ phase at $T \simeq 1000$ K and transforms into the face-centered cubic (fcc) γ phase at $T \simeq 900$ K. Near room temperature, the γ phase transforms into the double-hexagonal close-packed (dhcp) β phase. A further decrease in temperature results in the $\beta \rightarrow \alpha$ transition, where α-Ce is a low-volume fcc phase. It has been known for many years that x-ray diffraction shows that the γ and α phases are isostructural [6,7]. Recently a symmetry breaking was reported, where the α phase forms a quadrupolar-ordered variation on an fcc lattice with $Pa\bar{3}$ symmetry, as measured by nuclear perturbed angular correlation spectroscopy [8].

The phase equilibria near room temperature involve competition between thermodynamic and kinetic equilibrium between the γ and the β phases. This competition has direct bearing on the standard state of cerium. Based on a series of third-law calorimetry experiments carried out 20 years apart, the β phase was shown to slowly transform ($\sim$80 years) into the γ phase at room temperature and ambient pressure [9]. The present study is motivated by the realization that the presence of the β phase at room temperature in the phase diagram is metastable, and its relationship to the γ-to-α transition has not been described. It was anticipated that the stacking fault energies (SFEs) could explain the origin of defect motion and the presence of the metastable β phase.

Stacking faults are common crystalline defects. In face-centered cubic metals they can be seen as a disruption in the perfect stacking sequence $ABCABCABC\ldots$ in the (111) direction, the most common fault being the intrinsic stacking fault (isf) $ABCA|CABC\ldots$, where | indicates the position of the isf. The stacking fault energy is linked with the probability of errors in the stacking sequence of atomic layers in materials and sets the width of the ribbon formed by the Schockley partials. This energy has been correlated with several important mechanical properties like hardening, twin formation, and plasticity [10,11]. Insight into factors driving the above-mentioned phase equilibria can be gained by examining the cerium crystallography (see Fig. 1). With the exception of a stacking fault, the β phase has a crystal structure nearly identical to that of to the γ and α phases and may be represented as a close-packed structure with the stacking sequence going as $ABACAB$ (Fig. 1). Altogether it is difficult to distinguish the influence of the β phase on the γ-to-α transition, compounded by the fact that, outside of a few papers, there are few data to draw upon. It has been shown [12] by electron energy-loss spectroscopy that even though γ- and β-Ce are similar in volume and atomic coordination number, their spectral features differ, indicating that changes in the (111) stacking sequence might influence the electronic structure.

The repeated transformation of γ-Ce to α-Ce induces plastic deformation in the crystal, thereby retarding the transition [13]. It has been argued [14] that the repeated cycling between the γ and the α phases would introduce dislocations. Because the stacking fault energy has a close correlation with the mechanical properties and deformations, our efforts have been directed at a thorough calculation of the SFEs for cerium

*andreas.oestlin@physik.uni-augsburg.de

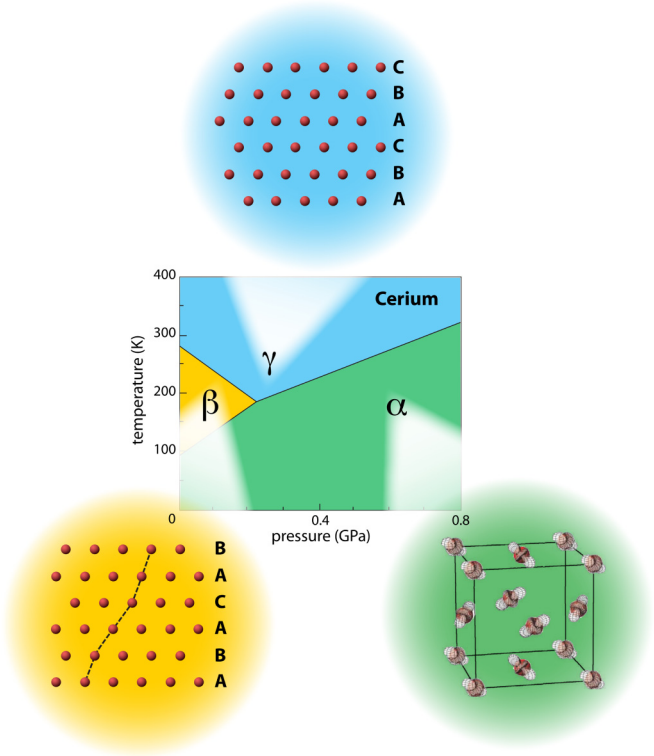

FIG. 1. Cerium phase diagram near ambient temperature and pressure. The crystal structures and stacking arrangements of the γ, β, and α phases are shown. The structure of the γ phase is projected along the close-packed (111) planes (horizontal rows of atoms) in the [110] direction to emphasize the stacking sequences. The structure of the β phase is shown along the close-packed (001) planes in the [100] direction. The possible orbital ordering is shown for the α structure, as determined by nuclear perturbed-angular-correlation spectroscopy [8].

using density functional theory (DFT) [15,16]. To validate our results we have also performed selected simulations based on the dynamical mean-field theory (DMFT) and the disordered local moment (DLM) approach. We show that there are large differences in the SFEs between the γ and the α phases. These differences are coupled to the order parameter of the transition. It was determined that the dhcp β phase is nearly degenerate with the fcc γ phase at zero pressure. These results agree with third-law calorimetry, which shows a slow reversion of the β phase into the thermodynamically stable γ phase. We comment on the similarity of this problem to the sluggish transformation of fcc-stabilized δ-plutonium alloys into a euctectic mixture of Pu_3Ga and monoclinic plutonium [17].

II. COMPUTATION TECHNIQUES

The intrinsic stacking fault energy is defined as the energy needed to create the intrinsic stacking fault in an otherwise perfect fcc stacking sequence. The formation energy needed to create an intrinsic stacking fault at ambient pressure can be expressed as

$$\gamma_{\mathrm{isf}} = \frac{E_{\mathrm{isf}} - E_0}{A}, \tag{1}$$

where E_{isf} and E_0 are the total energies for the system with and without stacking faults, and A is the area of a stacking fault. Several methods have been used to calculate γ_{isf} using an *ab initio* approach. The supercell method provides a direct route to calculate the energies of the stacking faults [18]. Here we have also used the axial interaction model (AIM), which maps the interaction between stacking layers to an Ising-type model [19,20]. The AIM makes it possible to elucidate the dependence of the SFE on energy differences between close-packed structures. It has previously been used to study stacking fault energies in transition metals [21], binary alloys [22], and ternary steel alloys [23]. The mapping gives rise to an infinite sum of interaction parameters between layers, one sum for each kind of stacking sequence. Truncation of these sums to second order in the interaction parameters, and subsequent elimination of the interaction parameters, gives a first approximation to the SFE as

$$\gamma_{\mathrm{isf}}^{\mathrm{2nd}} = \frac{2(E_{\mathrm{hcp}} - E_{\mathrm{fcc}})}{A}, \tag{2}$$

while going to third order gives

$$\gamma_{\mathrm{isf}}^{\mathrm{3rd}} = \frac{E_{\mathrm{hcp}} + 2E_{\mathrm{dhcp}} - 3E_{\mathrm{fcc}}}{A}. \tag{3}$$

E_{fcc}, E_{hcp}, and E_{dhcp} are the total energies for the fcc, hexagonal close-packed (hcp; having $ABABAB\ldots$ stacking), and dhcp structures. The calculations were done by first determining the fcc (111)-plane lattice constant $a_{\mathrm{fcc}}^{(111)} \equiv a_{\mathrm{fcc}}/\sqrt{2}$ by a volume minimization. The fcc (111) plane imposes a constraint on the faulted area [24]. Hence, energy differences for the hcp and dhcp structures were obtained by optimizing the c lattice constant, while keeping the in-plane lattice constant fixed, so that $a_{\mathrm{hcp}} = a_{\mathrm{dhcp}} = a_{\mathrm{fcc}}^{(111)}$.

The next issue is to find a method that can be used to calculate the needed energies for the AIM model and the supercell. For cerium, several procedures have been developed over the years in order to correctly capture the α-γ phase transition. Using only conventional exchange-correlation functionals within DFT, like the local density approximation (LDA) or the generalized gradient approximation (GGA), the volume collapse cannot be easily reproduced, however, it is possible to model the two cubic phases separately. Traditionally, this was done by assuming that the f electron in α-Ce is itinerant and is part of the valence band, while in γ-Ce the f electron is in the atomic core. This approach has been employed many times, giving reliable results with respect to equilibrium properties [25–27]. However, this approach exhibits several differences from data obtained from spectroscopy [28,29]. One is the absence of a quasiparticle peak at the Fermi level, a feature observed for both the α and the γ phase. In recent decades, extensions of DFT with DMFT [30] have proven to be able to accurately describe systems where electronic correlations are of importance. There exist several studies of cerium where this approach is employed, using different ways to solve the DMFT impurity problem [33–37]. These studies all provide an improved description of many equilibrium properties as well as the spectral functions and, also, shed light on the origin of the volume collapse transition. However, these methods deviate from the *ab initio* approach in that they depend on external parameters such as the Hubbard Coulomb

term U, choice of double counting correction, and method used to choose the correlated orbital subset. The solution of the effective impurity problem introduces additional errors, which make it difficult to reach the required precision for stacking fault energies [38]. In light of these disadvantages, and given that we are mainly interested in stacking fault energies for α-Ce and γ-Ce separately, we find it more convenient to use conventional density functional theory for the main core of our study. To analyze the role of strong correlations we have also performed selected DMFT calculations, as described below.

The main part of the calculations were done using the Vienna Atomistic Simulation Package (VASP) [31]. This package uses a projected augmented wave (PAW) basis set. The exchange-correlation functional was computed within the GGA [32], using the Perdew-Burke-Ernzerhof parametrization [39]. In a previous study [40] the LDA [41] of the exchange-correlation functional has been shown to give equilibrium properties for the lanthanides farther away from the experimental values than the Perdew-Burke-Ernzerhof parametrization does. We have performed a few calculations with the LDA as a frame of reference. The **k**-point sampling for the fcc structure was done utilizing a $29 \times 29 \times 29$ uniform mesh centered at the Γ point, and a $29 \times 29 \times 23$ mesh was used for hexagonal structures. A tetrahedron method containing Blöchl corrections [42] was used to handle the **k**-point integration. A cutoff energy of 500 eV was used for the wave functions. Spin-orbit coupling was neglected for the valence electrons. Equilibrium volumes and bulk moduli were computed for a number of volumes around the minimum energy and were fit to a Morse equation of state [43]. Supercells consisted of 12 layers and were constructed following Ref. [18] and using ideal fcc packing between (111)-plane layers. We treated the $4f$ electron in α-Ce as an itinerant valence electron using a PAW potential with valence configuration $6s^2 5d^1 f^1$. No attempt was made to model the quadrupolar-ordered structure, and the site symmetry was spherical in α-Ce. The $4f$ electron in the γ phase was regarded as localized. Hence we treated the $4f$ electron as a core electron by using a PAW potential with valence configuration $6s^2 5d^1 f^0$. The $5s^2$ and $5p^6$ states were treated as semicore states for both potentials. In the following, we denote the potential used to model α-Ce as the α potential and the potential used to model γ-Ce as the γ potential.

To explore the effect of strong electronic correlations on our results, we also performed additional calculations based on density functional theory calculations merged with dynamical mean-field theory (DFT + DMFT). We have used the electronic structure code RSPt [44,45], which is based on the full-potential linear muffin-tin orbital (FPLMTO) method and is particularly suitable for heavy elements such as lanthanides and actinides. Given that we intend to model the α and γ phases separately, we used two distinct solvers for the effective impurity model arising in DMFT. This procedure is aimed at describing the localized versus itinerant regimes and has been successfully applied to the Ce pnictides and γ Ce itself, giving good results for both spectral and ground-state properties [46]. γ-Ce was considered within the Hubbard I approximation (HIA) [47] and the Hubbard U was set to $U = 7$ eV, in agreement with previous studies [48,49]. The Hund's exchange J was calculated by using partially screened Slater integrals [48], which gave a value of $J = 0.786$ eV. α-Ce was addressed through the spin-polarized T-matrix fluctuation-exchange (SPTF) solver [50], and the Coulomb interaction parameters were chosen to be $U = 4.5$ eV and, again, $J = 0.786$ eV. The drastic reduction in the value of U for the α phase is motivated by that the SPTF solver is known to overestimate the strength of correlation effects, due to underscreening of the Coulomb interaction [52]. Within this approach, GGA + DMFT simulations were carried out with full convergence over both self-energy and electron density. More details on the computational scheme, including the constructions of the local orbitals, can be found elsewhere [46,51]. The FPLMTO basis set was set up to include $6s$, $6p$, $5d$, and $4f$ electrons, as well as the semicore states $5s$ and $5p$. The $5f$ states have also been added to increase the flexibility of the basis. Three kinetic energy tails were considered for $6s$ and $6p$ states, while only two were used for the rest. We used 726, 2048, and 3703 **k**-points (in the full Brillouin zone), respectively, for the hcp, fcc, and dhcp structures. DMFT simulations were carried out at a temperature of 400 K, using a total of 2048 fermionic Matsubara frequencies.

γ-Ce has been shown to exhibit paramagnetism following the Curie-Weiss law, while α-Ce behaves as a Pauli paramagnet [1]. DMFT can capture the paramagnetic metal phase. We also examined the paramagnetic phase of γ-Ce in a second way, with the exact muffin-tin orbital (EMTO) method [53–55]. Here the f electron was treated as a core electron and placed in one of the spin channels, making the core electron density spin-polarized. The core was kept frozen during the self-consistent iterations, while the valence states where treated making use of the disordered local moment approach within the coherent potential approximation [56]. Random fluctuations of the local moment were modeled by a substitutional alloy with two spin channels, $Ce_{0.5,\uparrow}Ce_{0.5,\downarrow}$, where the arrows indicate the different spin channels. Note that this method assumes an ideal paramagnet, i.e., no interaction between neighboring spins takes place and completely ignores any magnetic short-range order effect. On the other hand, the EMTO-DLM allows for surviving atomic (local) moments embedded in a nonpolarized effective medium. The valence density and Fermi level were found by complex contour integration using a semicircle of diameter 1.8 Ry with 32 integration points. The $5s^2$ and $5p^6$ states were treated as semicore states. The angular momentum states included in the valence were s, p, and d. Between 500 and 600 **k**-points, depending on the structure, were used for the integration in the irreducible Brillouin zone, and the LDA was used for the exchange-correlation potential.

The Appendix provides a comparison among the three basis sets used in this study.

III. RESULTS

A. Equilibrium properties

Equilibrium volumes and bulk moduli were computed to validate our approach. Values for α-Ce, together with data taken from Ref. [27] and experimental results, are listed in Table I. The GGA is seen to underestimate the experimental

TABLE I. Calculated and experimental volume (Å^3), bulk modulus B_0 (GPa), and stacking fault energies (mJ/m^2) of α-Ce and γ-Ce. Calculations were done using the GGA for the exchange-correlation potential.

	α-Ce			γ-Ce		
	Expt.	This work	Ref. [27]	Expt.	This work	Ref. [27]
Volume	28.17	26.47	27.74	34.36[a]	37.72	37.31
B_0	20–24,[b] 29[a]	39	39.1	19[c]	30	28.8
$\gamma_{\text{isf}}^{\text{2nd}}$		301			58	
$\gamma_{\text{isf}}^{\text{3rd}}$		311			16	
$\gamma_{\text{isf}}^{\text{supercell}}$		369			−0.2	

[a]From Ref. [57].
[b]From Ref. [58].
[c]From Ref. [61].

volume, while overestimating the bulk modulus. Similar results have been observed earlier for α-Ce [59,60], where different basis sets were used. In parallel with the GGA the LDA for the exchange-correlation potential was also investigated for the α potential. In this case the equilibrium volume becomes 22.98 Å^3 and the bulk modulus becomes 58 GPa, showing that these quantities are farther away from experiment. As shown in Sec. III B, the LDA still gives structural energy differences that are similar to those of the GGA.

A second-order AIM approximation gives an intrinsic SFE $\gamma_{\text{isf}}^{\text{2nd}} = 301$ mJ/m^2, while a third-order approximation gives $\gamma_{\text{isf}}^{\text{3rd}} = 311$ mJ/m^2. A direct supercell approach yields $\gamma_{\text{isf}}^{\text{supercell}} = 369$ mJ/m^2. The difference between the AIM and the supercell results could possibly be attributed to the use of ideal stacking in the supercell; i.e., the structure was not fully relaxed. This would introduce internal strain in the supercell, increasing its energy. We found that the c/a ratios of the hexagonal structures are relatively high at low volumes. This would indicate larger deviations from the ideal stacking around the stacking fault in α-Ce.

Calculated equilibrium results for γ-Ce are listed together with data from other sources in Table I. The γ-Ce potential along with the cited results tend to overestimate the volume and bulk modulus. A second-order approximation gives an intrinsic SFE $\gamma_{\text{isf}}^{\text{2nd}} = 58$ mJ/m^2, while going to the third order leads to $\gamma_{\text{isf}}^{\text{3rd}} = 16$ mJ/m^2. Inspection of the result from the supercell $\gamma_{\text{isf}}^{\text{supercell}} = -0.2$ mJ/m^2 demonstrates that the SFE is lowered even further and becomes 0 within the numerical accuracy of our calculations. The large decrease in SFE between second and third order in the AIM can be understood by examining Eqs. (2) and (3), where the latter equation contains the energy of the dhcp structure, while the former does not. In the case of γ-Ce, the dhcp-fcc energy difference is −0.4 mRy, indicating that the dhcp structure is nearly degenerate with the fcc structure, similar to lanthanum [62]. Note that the Debye temperature has been determined experimentally as 131 K for β-Ce and 127 K for γ-Ce [63]. The difference in the Debye temperatures comes close to stabilizing γ-Ce over the β phase at experimental volume and room temperature [64]. This result can be inferred from third-law calorimetry [9], which shows that β-Ce transforms into γ-Ce, albeit slowly.

B. Energy differences

There is a marked increase in the SFE as the system goes from the γ to the α phase. Two main mechanisms are responsible. The stacking fault area A decreases, and the structural energy difference between fcc and hexagonal lattices increases, as $\gamma \rightarrow \alpha$. This highlights the importance of structural energy differences that have been used in the determination of the SFE, as can be seen by inspection of the AIM approximations, Eqs. (2) and (3). The dependence can be better illustrated by rewriting Eqs. (2) and (3) as

$$\gamma_{\text{isf}}^{\text{2nd}} = \frac{2\Delta E_{\text{hcp}}}{A}, \tag{4}$$

$$\gamma_{\text{isf}}^{\text{3rd}} = \frac{\Delta E_{\text{hcp}} + 2\Delta E_{\text{dhcp}}}{A}, \tag{5}$$

where ΔE_{hcp} and ΔE_{dhcp} stand for the hcp-fcc and the dhcp-fcc energy differences. We investigated these differences as a function of the volume. Recall that the in-plane hexagonal lattice constant was kept fixed, while the c lattice constant was relaxed in the SFE calculations. If the in-plane lattice constant were to be decreased (increased) from its equilibrium value, the c lattice constant would drastically increase (decrease) to unphysical values, owing to the Poisson effect [65]. Therefore, in the following calculations, the in-plane and c lattice constants were relaxed as a function of the volume when ΔE_{hcp} and ΔE_{dhcp} were computed.

Figure 2 shows ΔE_{hcp} as a function of volume for the α and γ potentials within the GGA. The α potential (black squares) shows a maximum (∼6.5 mRy) around the calculated α-Ce volume. As the volume increases, ΔE_{hcp} decreases to around ∼2 mRy around the γ-Ce volume. A similar trend is seen for the γ potential (black triangles), with ΔE_{hcp} reaching a maximum (∼3 mRy) close to the α-Ce volume. If the volume is decreased below the equilibrium volume of α-Ce, ΔE_{hcp} decreases again. This effect has been reported in α-Ce, using the local density approximation for the exchange-correlation potential [66]. Therefore a larger volume (above V_α) will lead to a smaller ΔE_{hcp} and, hence, to a lower stacking fault energy. In Fig. 2, results from other procedures to model the α and γ potentials are also shown. Green circles correspond to the same electronic configuration as the GGA α potential, but within the LDA. As shown in the previous section, the LDA gave worse results for the equilibrium volume and bulk modulus compared

with the GGA. For the energy differences, however, no large discrepancy between the LDA and the GGA pseudopotentials can be seen.

The blue stars in Fig. 2 correspond to results from the FPLMTO + SPTF aimed at modeling the α phase. It is clear that the trend is the same as that obtained with the PAW method using the α potential. Hence, the trend of decreasing $\Delta E_{\rm hcp}$ is seen also for the DMFT results. We can now discuss the FPLMTO + HIA results for the γ phase. It was shown in a previous study [46] that the equilibrium volume and bulk modulus within the FPLMTO + HIA are in better agreement with experimental data than the present PAW data. However, as is clear from Fig. 2, the energy differences $\Delta E_{\rm hcp}$ are still rather similar to those obtained with the PAW for the γ potential. The two sets of data, the γ potential (black triangles) and the FPLMTO + HIA (red diamonds), differ in the steepness of the curve. However, it is not simple here to understand what is due to the DMFT corrections and what is due to differences in different electronic structure codes. In fact, even parent FPLMTO simulations, i.e., before the DMFT correction is applied, exhibit a steeper curve than the α potential (see the Appendix). This may be due to the inherent differences between a full electron code and a PAW code, as well as to the different treatments of spin-orbit coupling.

We should note here that if we were using an exact method Fig. 2 should report only a single curve going from the γ-Ce volume to the α-Ce volume. We use a twofold approach aiming at describing the two phases around their own volumes. We can expect the physical curve to be located in the region included between our curves.

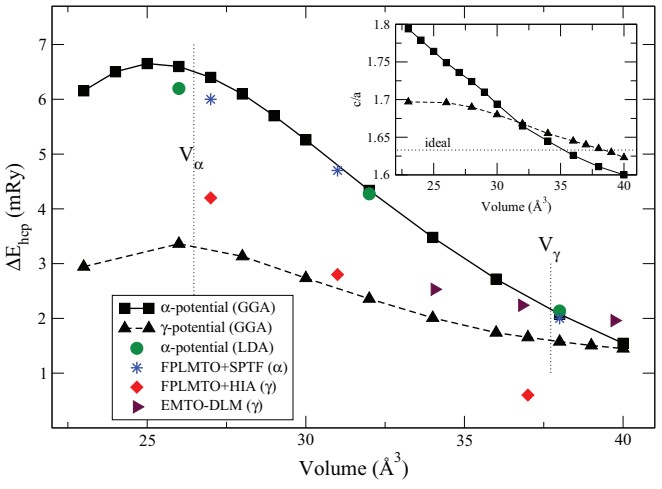

FIG. 2. $\Delta E_{\rm hcp} = E_{\rm hcp} - E_{\rm fcc}$ as a function of volume for both the α (black squares, solid line) and the γ (black triangles, dashed line) potentials, within the GGA. Calculated equilibrium volumes for α-Ce, V_α, and γ-Ce, V_γ, are represented by dotted lines. Energy differences calculated within the LDA for the α potential are shown by green circles. Results from the FPLMTO + DMFT, utilizing the SPTF and HIA impurity solvers, are represented by blue stars and red diamonds, respectively. Values from the EMTO-DLM treatment of the paramagnetic phase of γ-Ce are shown as maroon triangles. Inset: c/a ratio as a function of volume for both potentials. The ideal c/a ratio ($\sim$1.633) is shown by the dotted line.

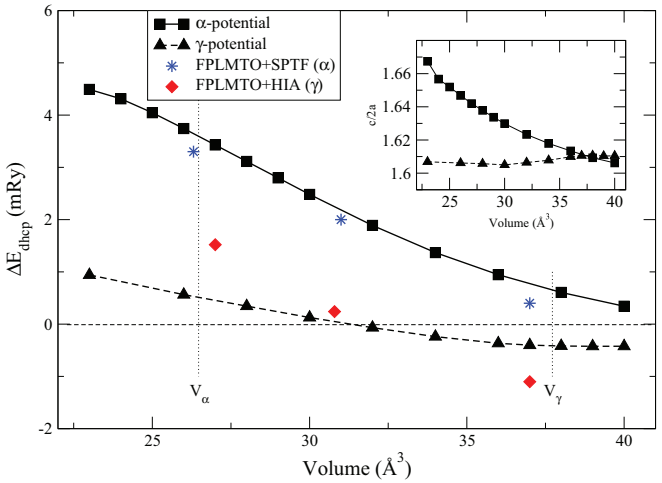

FIG. 3. $\Delta E_{\rm dhcp} = E_{\rm dhcp} - E_{\rm fcc}$ as a function of the volume for both the α (squares, solid line) and the γ (triangles, dashed line) potentials, the FPLMTO + DMFT with the SPTF solver (blue stars), and the FPLMTO + DMFT with the HIA impurity solver (red diamonds). Calculated equilibrium volumes for α-Ce, V_α, and γ-Ce, V_γ, are represented by dotted lines. Inset: $c/2a$ ratio as a function of the volume for both potentials.

In order to determine whether magnetism has any effect on the energy differences, we treated γ-Ce as a paramagnet within the EMTO-DLM approximation (see maroon triangles in Fig. 2). The energy differences $\Delta E_{\rm hcp}$ between the non-magnetic EMTO method calculations and the paramagnetic calculations were of the order of $\lesssim$0.1 mRy, and hence the paramagnetic behavior hardly changes the above picture. It was noted in the calculations that the polarization of the core density gave only a small exchange splitting of the valence states, of the order of $\sim$0.05 μ_B, which gives a change in the total energy of the order of $\sim$1 mRy and lower for structural energy differences. The $\Delta E_{\rm hcp}$ calculated within the EMTO-DLM method is roughly $\sim$0.5 mRy larger compared to the PAW results (dashed line), however, the slope of the curve is basically the same, indicating a similar trend. To briefly summarize, the trend of a decreasing hcp-fcc energy difference (and hence decreasing stacking fault energy) seems to be quite robust with regard to the choice of how to model the α and γ phases.

In Fig. 3, $\Delta E_{\rm dhcp} = E_{\rm dhcp} - E_{\rm fcc}$ can be seen for both the α (black squares) and the γ (black triangles) potentials as a function of the volume. The same trends (decreasing energy difference with increasing volume) as for the hcp case are seen. Around the equilibrium volume of α-Ce, the α potential gives an energy difference $\Delta E_{\rm dhcp} \sim 3.5$ mRy, which is roughly half that of $\Delta E_{\rm hcp}$ at the same volume. Referring to Eq. (5) for the third-order SFE in the AIM, it can be seen that this indicates that there should not be a large change in the SFE upon going from second to third order in the AIM. This is indeed the case since $\gamma_{\rm isf}^{\rm 2nd} = 301$ mJ/m^2 and $\gamma_{\rm isf}^{\rm 3rd} = 311$ mJ/m^2 for α-Ce in the AIM (see Table I). For the γ potential, the magnitude of $\Delta E_{\rm dhcp}$ is $\lesssim$ 1 mRy for the whole volume range. This makes the dhcp and fcc structures nearly degenerate and gives a low SFE for γ-Ce according to the AIM.

In Fig. 3 we also show ΔE_{dhcp} calculated using energies from the FPLMTO + DMFT approach, using the SPTF (blue stars) and the HIA (red diamonds) as the impurity solver. Using the FPLMTO + DMFT approach, a trend similar to that for ΔE_{hcp} can be seen upon comparison with the PAW results; i.e., a steeper energy difference curve is observed as a function of volume for γ-Ce.

IV. DISCUSSION

The role of the SFE on the γ-α transition is of interest. It has been known that the phase diagram of Ce shows signs of pressure and temperature hysteretic effects [1,13]. If γ-Ce is held at room temperature and subjected to hydrostatic pressure, it transforms to α-Ce at $\sim$0.8 GPa. Once the pressure is released, the α-Ce will transform back to the γ phase at $\sim$0.6 GPa. The hysteretic region in the cerium temperature-pressure phase diagram is wedge shaped, with an apex located at the critical point (C.P.) [1] (see Fig. 4). This wedge is broadened as the temperature is lowered and, finally, reaches its base when it enters the metastable β phase. It was shown by Moore *et al.* [14] that the γ-α transition preserves the crystal orientation of the fcc structure. The resulting cerium crystal would have to form an interface between the host and the precipitates. Owing to the volume mismatch between the two phases, dislocation lines would have to be introduced at the interface. When going from $\gamma \rightarrow \alpha$, creating dislocations in both phases is relatively easy due to the low SFE (Fig. 2). Instead, when going from $\alpha \rightarrow \gamma$, the formation of dislocations is energetically more costly than before due to the large SFE that delays the phase transformation. Hence, to a large extent the pressure hysteresis should be attributed to the very strong volume and phase dependence of the SFE.

A decreasing volume (increasing pressure) will lead to an increase in the SFE, making dislocation emission more problematic. Since it is about 30% easier to compress the γ phase compared to the α phase (Table I), an intermediate pressure ($\lesssim$1.5–2 GPa) will have a larger SFE-enhancing effect on the gamma phase, bringing the two SFEs close to each other and thus reducing the width of the hysteretic region. However, at very low pressures this mechanism is less effective, and the large difference between the two SFE values creates large stresses upon the phase transition. This raises an interesting hypothesis in that the β phase acts as a dislocation reservoir to accommodate the strain caused by the α-γ transition. The dhcp phase is a mixture of fcc and hcp lattices, and its energy difference, relative to fcc, is smaller than the difference between hcp and fcc. The β phase is barely stable on energetic grounds, and we surmise that stacking faults can accommodate dislocations generated as a result of the large volume mismatch between α and γ-Ce. The sluggish transformation of β-Ce into γ-Ce is reminiscent of the slow ($t_{1/2} = 5500$ years) decomposition of fcc-stabilized plutonium phases into a eutectoid [17]. In this case the thermodynamic driving forces are favorable for pushing δ-Pu into a eutectic mixture containing Pu_3Ga and α-Pu. However, the deformation and dislocation formations in δ-Pu suggest that kinetics compete with thermodynamic equilibrium conditions.

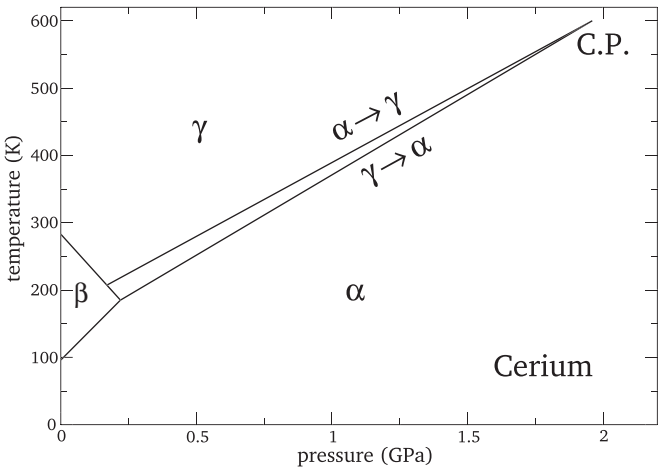

FIG. 4. Cerium pressure-temperature phase diagram showing the hysteresis during the $\gamma \rightleftharpoons \alpha$ transition. The line corresponding to the $\gamma \rightarrow \alpha$ transition and the domain of the β phase was taken from the data in Ref. [9]. The line corresponding to the $\alpha \rightarrow \gamma$ transition was estimated from data in Ref. [13].

V. CONCLUSION

In summary, total formation energies for cerium were computed using an axial interaction model that maps the interaction between stacking layers to an Ising-type model. We find a large difference in the stacking fault energies between the α and the γ phases and a β-phase energy that is nearly degenerate with the γ phase. Our work represents a step toward the understanding of dislocations in cerium, which is still a largely unexplored area. In each of the computational approaches used here one can argue about specific assumptions and limitations, but the fact that all calculations produce the same trend gives us confidence in the overall approach. Although we do not expect significant differences for the α and γ phases separately, the transition from one energy difference curve to another, which is expected to happen in between the two equilibrium volumes, needs to be better clarified to analyze the detailed relation between the electronic correlation and the stacking fault energies.

ACKNOWLEDGMENTS

We thank Börje Johansson, Bob Albers, Angus Lawson, and Jon Lawrence for helpful discussions. A.Ö. and L.V. acknowledge financial support from the Swedish Research Council, the Swedish Foundation for Strategic Research, and the Hungarian Scientific Research Fund (research projects OTKA 84078 and 109570). I.D.M. and I.L. acknowledge financial support from the Swedish Research Council and the Knut and Alice Wallenberg Foundation (research projects of Prof. Olle Eriksson). Computations were performed using resources provided by the Swedish National Infrastructure for Computing (SNIC) at the National Supercomputer Centre in Linköping and at the PDC Center for High Performance Computing in Stockholm. Work at the Los Alamos National Laboratory was carried out under the auspices of the United States Department of Energy.

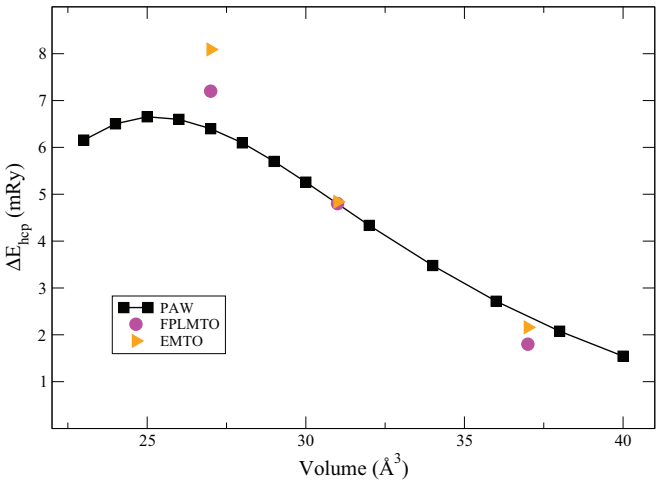

FIG. 5. Comparison between $\Delta E_{\rm hcp} = E_{\rm hcp} - E_{\rm fcc}$ from the different basis sets used in this study, each employing the α-potential (the f-electron is treated as a valence electron). The black curve corresponds to the PAW method, the magenta circles correspond to the full-potential LMTO method and the orange triangles correspond to the EMTO method.

APPENDIX: BASIS SET COMPARISON

In this study, we based our calculations on three basis sets. The reason for this is twofold. First, the DMFT and the coherent potential approximation extensions are not available at the same time in a single electronic structure program package, making it necessary to use more than one program package. Second, this gives us a measure of how sensitive our results are with regard to the choice of basis set. To be able to compare the different methods used in this work, Fig. 5 shows the quantity $\Delta E_{\rm hcp} = E_{\rm hcp} - E_{\rm fcc}$ as a function of the volume for α-Ce (with the f electron treated as a valence electron) for the three methods. $\Delta E_{\rm hcp}$ was chosen because it is an important quantity within the axial interaction model, as seen from Eq. (4). Compared to the PAW pseudopotential method (black squares, solid line), the all-electron muffin-tin methods FPLMTO (magenta circles) and EMTO (orange triangles) overestimate $\Delta E_{\rm hcp}$ for low volumes and underestimate it for high volumes. Overall, the agreement between the methods is good. The largest deviation from the full-potential PAW result is given by the EMTO method at a low volume, where the deviation is $\sim$2 mRy. One possible reason for this deviation is the spherical approximation of the effective potential made in the EMTO method. At low volumes, the relaxed c/a ratio for the hcp structure is fairly high ($\sim$1.75; see inset in Fig. 2) compared to the ideal ratio ($\sim$1.63). This high c/a ratio gives a crystal structure that might not be suitable for modeling within the spherical approximation. However, in this work the EMTO method was used to model cerium at large volumes where the c/a ratio is closer to the ideal (see inset in Fig. 2), making the spherical approximation suitable.

[1] D. C. Koskenmaki and K. A. Gschneidner, Jr., *Handbook on the Physics and Chemistry of Rare Earths, Vol. 1*, edited by K. A. Gschneidner, Jr. and L. Eyring (North-Holland, Amsterdam, 1978).

[2] B. Johansson, Philos. Mag. **30**, 469 (1974).

[3] J. W. Allen and R. M. Martin, Phys. Rev. Lett. **49**, 1106 (1982).

[4] P. W. Bridgman, *The Physics of High Pressures* (G. Bell and Sons, London, 1931).

[5] B. Johansson, E. Luo, S. Li, and R. Ahuja, Sci. Rep. **4**, 6398 (2014).

[6] A. W. Lawson and T.-Y. Tang, Phys. Rev. **76**, 301 (1949).

[7] F. Decremps, L. Belhadi, D. L. Farber, K. T. Moore, F. Occelli, M. Gauthier, A. Polian, D. Antonangeli, C. M. Aracne-Ruddle, and B. Amadon, Phys. Rev. Lett. **106**, 065701 (2011).

[8] A. V. Tsvyashchenko, A. V. Nikolaev, A. I. Velichkov, A. V. Salamatin, L. N. Fomicheva, G. K. Ryasny, A. A. Sorokin, O. I. Kochetov, M. Budzynski, and K. H. Michel, Phys. Rev. B **82**, 092102 (2010).

[9] K. A. Gschneidner and V. K. Pecharsky, J. Phase Equilib. **20**, 612 (1999).

[10] M. Ahlers, Met. Mater. Trans. B **1**, 2415 (1970).

[11] M. Jo, Y. M. Koo, B.-J. Lee, B. Johansson, L. Vitos, and S. K. Kwon, Proc. Natl. Acad. Sci. USA **111**, 6560 (2014).

[12] K. T. Moore, B. W. Chung, S. A. Morton, A. J. Schwartz, J. G. Tobin, S. Lazar, F. D. Tichelaar, H. W. Zandbergen, P. Söderlind, and G. van der Laan, Phys. Rev. B **69**, 193104 (2004).

[13] E. G. Zukas, R. A. Pereyra, and J. O. Willis, Metall. Trans. A **18A**, 35 (1987).

[14] K. T. Moore, L. Belhadi, F. Decremps, D. L. Farber, J. A. Bradley, F. Occelli, M. Gauthier, A. Polian, and C. M. Aracne-Ruddle, Acta Mater. **59**, 6007 (2011).

[15] P. Hohenberg and W. Kohn, Phys. Rev. **136**, B864 (1964).

[16] W. Kohn and L. J. Sham, Phys. Rev. **140**, A1133 (1965).

[17] S. S. Hecker and L. F. Timofeeva, Los Alamos Sci. **26**, 244 (2000).

[18] S. Kibey, J. B. Liu, D. D. Johnson, and H. Sehitoglu, Acta Mater. **55**, 6843 (2007).

[19] P. J. H. Denteneer and W. van Haeringen, J. Phys. C **20**, L883 (1987).

[20] C. Cheng, R. J. Needs, and V. Heine, J. Phys. C **21**, 1049 (1988).

[21] N. M. Rosengaard and H. L. Skriver, Phys. Rev. B **47**, 12865 (1993).

[22] L. Song, Q.-M. Hu, E. K. Delczeg-Czirjak, B. Johansson, and L. Vitos, Acta Mater. **60**, 4506 (2012).

[23] L. Vitos, P. A. Korzhavyi, and B. Johansson, Phys. Rev. Lett. **96**, 117210 (2006).

[24] L. Song, Q. M. Hu, B. Johansson, and L. Vitos, Acta Mater. **59**, 5728 (2011).

[25] B. I. Min, H. J. F. Jansen, T. Oguchi, and A. J. Freeman, Phys. Rev. B **34**, 369 (1986).

[26] M. Krisch, D. L. Farber, R. Xu, D. Antonangeli, C. M. Aracne, A. Beraud, T.-C. Chiang, J. Zarestky, D. Y. Kim, E. I. Isaev, R.

Ahuja, and B. Johansson, Proc. Natl. Acad. Sci. USA **108**, 9342 (2011).
[27] B. Johansson, I. A. Abrikosov, M. Aldén, A. V. Ruban, and H. L. Skriver, Phys. Rev. Lett. **74**, 2335 (1995).
[28] M. Grioni, P. Weibel, D. Malterre, Y. Baer, and L. Duó, Phys. Rev. B **55**, 2056 (1997).
[29] J. W. van der Eb, A. B. Kuz'menko, and D. van der Marel, Phys. Rev. Lett. **86**, 3407 (2001).
[30] G. Kotliar, S. Y. Savrasov, K. Haule, V. S. Oudovenko, O. Parcollet, and C. A. Marianetti, Rev. Mod. Phys. **78**, 865 (2006).
[31] G. Kresse and J. Furthmüller, Phys. Rev. B **54**, 11169 (1996).
[32] J. P. Perdew, J. A. Chevary, S. H. Vosko, K. A. Jackson, M. R. Pederson, D. J. Singh, and C. Fiolhais, Phys. Rev. B **46**, 6671 (1992).
[33] K. Held, A. K. McMahan, and R. T. Scalettar, Phys. Rev. Lett. **87**, 276404 (2001).
[34] A. K. McMahan, K. Held, and R. T. Scalettar, Phys. Rev. B **67**, 075108 (2003).
[35] N. Lanatá, Y.-X. Yao, C.-Z. Wang, K.-M. Ho, J. Schmalian, K. Haule, and G. Kotliar, Phys. Rev. Lett. **111**, 196801 (2013).
[36] J. Bieder and B. Amadon, Phys. Rev. B **89**, 195132 (2014).
[37] B. Amadon and A. Gerossier, Phys. Rev. B **91**, 161103(R) (2015).
[38] R. C. Albers, N. E. Christensen, and A. Svane, J. Phys.: Condens. Matter **21**, 343201 (2009).
[39] J. P. Perdew, K. Burke, and M. Ernzerhof, Phys. Rev. Lett. **77**, 3865 (1996).
[40] P. Söderlind, O. Eriksson, B. Johansson, and J. M. Wills, Phys. Rev. B **50**, 7291 (1994).
[41] J. P. Perdew and Y. Wang, Phys. Rev. B **45**, 13244 (1992).
[42] P. E. Blöchl, O. Jepsen, and O. K. Andersen, Phys. Rev. B **49**, 16223 (1994).
[43] V. L. Moruzzi, J. F. Janak, and K. Schwarz, Phys. Rev. B **37**, 790 (1988).
[44] J. M. Wills, M. Alouani, P. Andersson, A. Delin, O. Eriksson, and O. Grechnyev, *The Full-Potential Electronic Structure Method and RSPt* (Springer, Berlin, 2010).
[45] A. Grechnev, I. Di Marco, M. I. Katsnelson, A. I. Lichtenstein, J. Wills, and O. Eriksson, Phys. Rev. B **76**, 035107 (2007).
[46] M. S. Litsarev, I. Di Marco, P. Thunström, and O. Eriksson, Phys. Rev. B **86**, 115116 (2012).
[47] P. Thunström, I. Di Marco, A. Grechnev, S. Lebègue, M. I. Katsnelson, A. Svane, and O. Eriksson, Phys. Rev. B **79**, 165104 (2009).
[48] S. Lebègue, A. Svane, M. I. Katsnelson, A. I. Lichtenstein, and O. Eriksson, Phys. Rev. B **74**, 045114 (2006).
[49] L. V. Pourovskii, B. Amadon, S. Biermann, and A. Georges, Phys. Rev. B **76**, 235101 (2007).
[50] L. V. Pourovskii, M. I. Katsnelson, and A. I. Lichtenstein, Phys. Rev. B **72**, 115106 (2005).
[51] O. Grånäs, I. Di Marco, P. Thunström, L. Nordström, O. Eriksson, T. Björkman, and J. M. Wills, Comput. Mater. Sci. **55**, 295 (2012).
[52] V. Drchal, V. Janis, J. Kudrnovsky, V. S. Oudovenko, X. Dai, K. Haule, and G. Kotliar, J. Phys.: Condens. Matter **17**, 61 (2005).
[53] O. K. Andersen, O. Jepsen, and G. Krier, in *Lectures on Methods of Electronic Structure Calculation* (World Scientific, Singapore, 1994), p. 63.
[54] L. Vitos, H. L. Skriver, B. Johansson, and J. Kollár, Comput. Mater. Sci. **18**, 24 (2000).
[55] L. Vitos, Phys. Rev. B **64**, 014107 (2001).
[56] B. L. Gyorffy, A. J. Pindor, J. Staunton, G. M. Stocks, and H. Winter, J. Phys. F **15**, 1337 (1985).
[57] J. Donohue, *The Structure of the Elements* (John Wiley & Sons, New York, 1974).
[58] J. S. Olsen, L. Gerard, U. Benedict, and J.-P. Itié, Physica B **133**, 129 (1985).
[59] P. Söderlind, O. Eriksson, B. Johansson, and J. M. Wills, Phys. Rev. B **52**, 13169 (1995).
[60] A. Landa, P. Söderlind, A. Ruban, L. Vitos, and L. V. Pourovskii, Phys. Rev. B **70**, 224210 (2004).
[61] B. Amadon, F. Jollet, and M. Torrent, Phys. Rev. B **77**, 155104 (2008).
[62] H. L. Skriver, Phys. Rev. B **31**, 1909 (1985).
[63] S. S. Agafonov, M. S. Blanter, V. P. Glazkov, V. A. Somenkov, and M. N. Shushunov, Phys. Met. Metallogr. **110**, 338 (2010).
[64] G. Grimvall, *Thermophysical Properties of Materials*, enlarg. rev. ed. (North-Holland, Amsterdam, 1999).
[65] A material with a positive Poisson ratio (the negative of the ratio of transverse to axial strain) tends to expand (contract) in the two directions perpendicular to the direction of compression (stretching).
[66] P. Ravindran, L. Nordström, R. Ahuja, J. M. Wills, B. Johansson, and O. Eriksson, Phys. Rev. B **57**, 2091 (1998).